Dynamic Analysis of a Six-Cable Parallel Robot for Automated Panelized Building Retrofits

Yifang Liu, Nolan W. Hayes, Diana Hun, and Bryan P. Maldonado

Buildings and Transportation Science Division, Oak Ridge National Laboratory,* United States of America

liuy5@ornl.gov, hayesnw@ornl.gov, hunde@ornl.gov, maldonadopbp@ornl.gov

Abstract -

Cable-Driven Parallel Robots (CDPRs) are highly suitable for automated panelized building retrofits, thanks to their compact footprint and high payload-to-weight ratio. A common CDPR configuration featuring eight cables, where the anchors form a rectangular prism in front of the building facade, offers a large wrench feasible workspace and good control versatility. However, installing upper anchor points requires additional support structures, such as towers or beams, increasing setup complexity and posing logistical challenges in construction settings. To mitigate these challenges, we propose a six-cable CDPR model specifically designed for automated panelized building retrofits. Although the feasible workspace is limited, our analysis shows that the proposed CDPR adequately covers the critical areas required for panel installation. To validate that the six-cable system can effectively transport the end effector to the desired installation pose, we calculated optimal trajectories based on a constrained dynamic model. The simulation results of the six-cable CDPR demonstrate promising potential for automated panelized building retrofits, effectively balancing simplicity, cost-effectiveness, and functionality.

Keywords -

CDPR; Panelized Envelope; Construction Robotics; Trajectory Optimization

1 Introduction

Building retrofits using panelized prefabricated envelopes substantially enhance the energy efficiency of a building. Traditional methods for installing panels in multi-story buildings typically rely on manual labor or crane hoisting, with panels being placed by hand [1]. However, these approaches are often hindered by labor shortages, high costs, and panel installation errors. Automating this process with robotics offers a promising solution to enhance efficiency, improve quality, and reduce the overall installation cost. Cable-Driven Parallel Robots (CDPRs) are well-suited for handling heavy payloads while maintaining a compact footprint. These attributes make them particularly effective for automated building retrofits using prefabricated panelized systems.

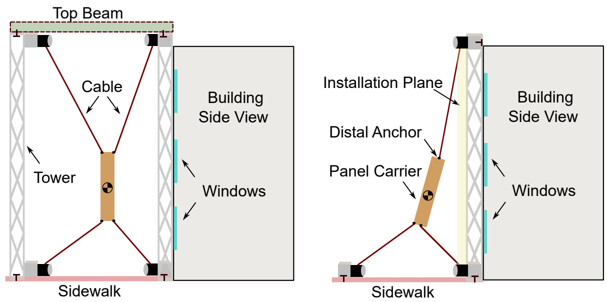

Figure 1. Side views of eight-cable (left) and six-cable (right) CDPRs for panelized building retrofits

CDPRs are highly versatile robotic systems used in various applications, including 3D printing [2], material handling [3], and prefabricated panel installation [4]. Many CDPR designs utilize an eight-cable configuration supported by rigid external elements surrounding the workspace [5]. This setup, with four anchor points on the ground and four positioned mid-air, offers a large wrench feasible workspace and high control versatility. However, installing the upper anchor points requires additional support structures, such as towers, cantilever beams, or bracing (left plot of Figure 1), which significantly increases setup complexity and presents logistical challenges in construction environments.

To address these issues, this paper introduces a novel six-cable CDPR model designed specifically for panelized building retrofits. As shown in the right plot of Figure 1, the proposed system uses six cables, with four anchors on the ground and two near the roof. By removing the anchor points that need to be suspended mid-air, this configuration simplifies setup process and mitigates logistical complexities. When the end-effector is away from the facade, the system operates as a spatial (three-dimensional) CDPR. However, as the center of mass of the end effector aligns with the installation plane, the bottom two cables furthest from the facade begin to sag, transitioning the system into a planar (two-dimensional) configuration. A key focus of this study is evaluating if the model is capable to transport the end effector from a starting feasible pose away from the facade (e.g., at the end of the sidewalk) to a desired pose at the installation plane near the facade. Using a dynamic model of the six-cable CDPR, a trajectory optimization problem was formulated to demonstrate the feasibility of the proposed design. Simulation results showed that the six-cable CDPR can successfully pick up a panel at a given pose and manipulate it to achieve the desired plumb and level panel position on the installation plane. To the best of our knowledge, this is the first six-cable configuration that is used for panelized building retrofits. This streamlined configuration aims to enhance feasibility and efficiency while maintaining sufficient operational control for panelized building retrofits.

The remaining sections are arranged as follows. Section 2 presents the state of the art in CDPRs for construction applications. Section 3 describes the benefits and challenges of a six-cables CDPR system. Section 4 defines the dynamic model used and the trajectory optimization problem to be solved. Section 5 demonstrates the simulation results. Section 6 concludes the paper and outlines directions for future work.

2 CDPRs in Construction Applications

Recently, CDPRs have gained attention across various fields and applications. Due to their desirable characteristics, such as scalability, reconfigurability, compact design, and high payload-to-weight ratio. They are widely investigated in construction applications such as bricklaying [6], 3D printing [7, 8], and solar power plant assembly [9]. Murphy *et al.* developed a planar CDPR for cooperative modular manipulation, enabling CDPRs to assist in construction tasks and gap-crossing scenarios [10]. For building envelope applications, Izard *et al.* explored the use of eight-cable CDPRs for inspecting building facades [11]. In addition, Iturralde *et al.* designed and implemented an eight-cable CDPR model for modular curtain wall installation in real-world applications [5]. Their work examined whether CDPRs could achieve sufficient accuracy for installing curtain wall modules and reduce manual installation time. In the context of automated panelized building retrofits, our previous work investigated the wrench feasible workspace for various cable configurations, with a primary focus on four-cable planar models and eight-cable 3D models [4]. CDPRs designed for building envelope applications have predominantly focused on eight-cable models, leaving the potential of a six-cable CDPR configuration unexplored.

3 Six-Cable CDPR for Panelized Systems

To achieve control over the six degrees of freedom (DOF) of the end effector, an eight-cable configuration is commonly used, especially when a large workspace is required. Among the eight proximal anchor points, two need to be placed away from the building facade and away from the ground. This setup usually requires additional support structures, such as vertical towers and/or top beams, as illustrated in Figure 1. Support towers provide a simplified setup by providing the necessary rigidity for the system while minimizing dependency on the building. In this case, if a CDPR with eight cables is needed, then four towers are required to attach all anchor points. Although top beams or bracing are not strictly mandatory, they become essential when a highly rigid support structure is needed. However, constructing four towers with beams and bracing presents logistical challenges and adds considerable expenses.

In contrast, some systems, such as Hephaestus [5], use only two welded-steel cantilever structural beams fastened to the roof of the building, with each beam element supporting two anchor points. While this approach reduces setup complexity, it is not universally applicable, particularly for older buildings where additional load-bearing capacity of the structure may be limited. The feasibility of relying solely on roof-mounted structures depends heavily on the building's age, structural integrity, and availability of attachment points. For such cases, a structural assessment is necessary to ensure that the building can support the CDPR system, which adds additional complexity and cost for retrofitting. To address these limitations and improve system robustness, we propose avoiding roof-mounted structures entirely, so that the CDPR design can be largely independent of the building's architecture.

Therefore, the tower-based setups, i.e. the combination of towers, top beams, and bracing, ensures a rigid and reliable system while minimizing dependence on the building structure itself to support the robot. Many existing multifamily residential buildings have sufficient space adjacent to the facade to accommodate the tower-based setups, which provides a suitable condition for retrofitting projects using CDPRs.

To further simplify the installation process and reduce costs, this paper investigates the feasibility of using a CDPR with only six cables for panelized building retrofits. This approach aims to maintain functionality while significantly minimizing the structural and logistical requirements associated with the traditional eight-cable configurations. The six-cable configuration offers several notable advantages. As illustrated in Figure 1, unlike the eight-cable setup that requires four top anchors, the six-cable

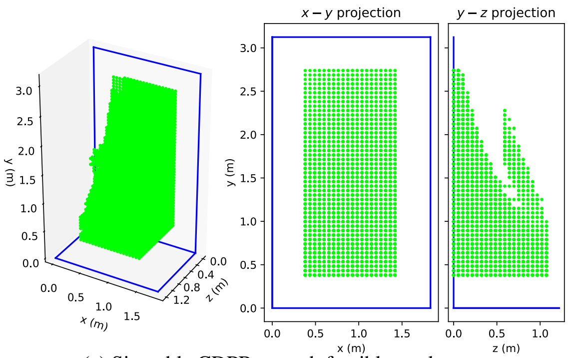

(a) Six-cable CDPR wrench feasible workspace

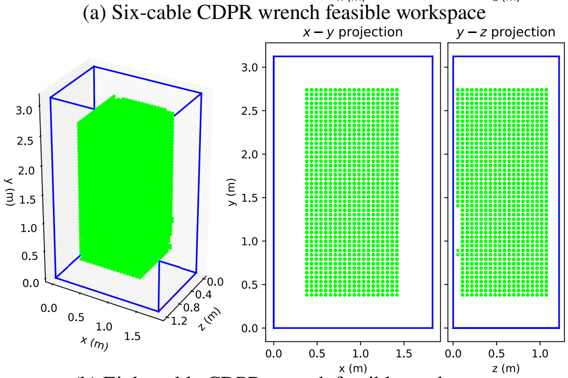

(b) Eight-cable CDPR wrench feasible workspace

Figure 2. Wrench feasible workspace of the six-cable CDPR and an eight-cable CDPR. Green dots represent feasible positions of the end effector's center of mass. Blue lines represent the CDPR frame. Left: 3D view; Middle: $x - y$ projection; Right: $y - z$ projection. Further details on the calculations can be found in Section 5.2.

system requires only two anchors located near the top of the building. This reduces the number of towers needed from four to two. Additionally, a six-cable CDPR system uses only six actuator systems, further lowering costs. The reduction in cables and towers minimizes material usage and overall expenses. These adjustments simplify the setup process and reduce installation complexity. However, this approach also introduces technical challenges. Unlike the eight-cable system, the six-cable configuration cannot provide sufficient control to achieve the same level of mobility for the end effector. This limitation reduces the workspace (see Figure 2), causing more than 30% of the wrench feasible area in the eight-cable CDPR to become wrench-infeasible. Additionally, it increases sensitivity to external disturbances and adds complexity to control and trajectory optimization. For example, in the eight-cable CDPR, when the end effector is at the pickup location, a wide range of initial orientations are wrench-feasible. However, for the six-cable CDPR, most of these initial orientations are no longer feasible. Additionally, determining

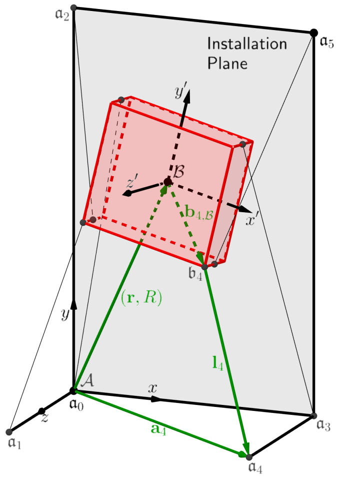

Figure 3. Geometric and dimensional definition of the six-cable CDPR model for building retrofits.

a feasible initial trajectory between a given starting position and target pose presents a significant challenge. This paper addresses these issues by proposing solutions to enhance the practicality and reliability of a six-cable CDPR. By overcoming these challenges, the six-cable configuration can serve as a promising alternative for certain retrofit applications, offering a balance between simplicity, cost-effectiveness, and functionality.

4 Modeling and Trajectory Optimization

We will start by describing the CDPR dynamic model and then formulating the trajectory optimization problem for bringing a panel from a starting pose to a desired pose.

4.1 CDPR Dynamics

The six-cable CDPR model studied in this paper is illustrated in Fig. 3. Note that in this setup, the installation plane is parallel to, but distinct from the building facade. The building facade is located on the negative side of the z axis. The fixed (black) frame of size $\boldsymbol{F} = \begin{bmatrix} F_x & F_y & F_z \end{bmatrix}^T$ sets the dimensions of the CDPR in the world coordinate system $\mathcal{A}$. The CDPR manipulates the (red) end effector of size $\boldsymbol{P} = \begin{bmatrix} P_{x'} & P_{y'} & P_{z'} \end{bmatrix}^T$, which defines the dimensions of the panel in the rotating coordinate system $\mathcal{B}$. Note that in real-world panel installation using CDPRs, the end effector serves as the panel carrier and may be bigger than the panel itself. Finally, $n = 6$ massless cables connect the panel to the frame. The cable end connected to the frame runs through pulleys and cable drums to facilitate the winding and unwinding of the cable. However, in this study, we will not model the geometry or dynamics of the winding mechanism. Consider the following vectors for $i \in \{1, \ldots, n\}$, according to Figure 3:

- The constant vectors $\mathbf{a}_i$ denote the proximal anchor points $\mathfrak{a}_i$ in the frame with respect to $\mathcal{A}$.
- The constant vectors $\mathbf{b}_{i,\mathcal{B}}$, denote the distal anchor points $\mathfrak{b}_i$ in the panel with respect to $\mathcal{B}$.
- The pose $(\boldsymbol{r}, R)$ is defined by the location of the panel's center of mass $\boldsymbol{r} = \begin{bmatrix} r_x & r_y & r_z \end{bmatrix}^T$ relative to $\mathcal{A}$, and the orientation of the panel's frame $\mathcal{B}$ relative to $\mathcal{A}$, denoted by the rotation matrix $R \in SO_3$.
- The cable vectors $\boldsymbol{l}_i = \mathbf{a}_i - (\boldsymbol{r} + R\mathbf{b}_{i,\mathcal{B}})$ which are functions of the panel pose calculated relative to $\mathcal{A}$.
- The cable forces $\boldsymbol{f}_i = f_i \boldsymbol{l}_i / \|\boldsymbol{l}_i\|$ with $f_i \geq 0$ tension acting on the cables ($\|\cdot\|$ denotes Euclidean norm).

The translational motion of the panel is defined in terms of the acceleration of its center of mass, which is measured from the inertial frame of reference $\mathcal{A}$. Therefore, the Newton equations of translational motion are [12]:

$$\frac{d}{dt}\boldsymbol{r} = \boldsymbol{v} \tag{1}$$

$$\frac{d}{dt}\boldsymbol{v} = \boldsymbol{g} + \frac{1}{m}\sum_{i=1}^{n} f_i \frac{\boldsymbol{l}_i}{\|\boldsymbol{l}_i\|} - \frac{\mu_{\boldsymbol{v}}}{m}\boldsymbol{v}. \tag{2}$$

Here, $\boldsymbol{v}$ is the velocity of the panel's center of mass, $\boldsymbol{g}$ is the acceleration due to gravity, m is the panel's mass, and $\mu_{\boldsymbol{v}}$ is a linear friction coefficient to provide damping. Since the coordinate system $\mathcal{B}$ moves with the panel, the rate of change in orientation and Euler equations of motion written with respect to the coordinate system $\mathcal{B}$ are [12]:

$$\frac{d}{dt}\boldsymbol{\Phi} = T\boldsymbol{\omega}_{\mathcal{B}}. \tag{3}$$

$$\begin{aligned} \frac{d}{dt}\boldsymbol{\omega}_{\mathcal{B}} = &-I_{\mathcal{B}}^{-1}\left(\boldsymbol{\omega}_{\mathcal{B}} \times I_{\mathcal{B}}\boldsymbol{\omega}_{\mathcal{B}}\right) \\ &+ I_{\mathcal{B}}^{-1}\sum_{i=1}^{n} f_i \left(\mathbf{b}_{i,\mathcal{B}} \times \frac{R^T\boldsymbol{l}_i}{\|\boldsymbol{l}_i\|}\right) - I_{\mathcal{B}}^{-1}\mu_{\omega}\boldsymbol{\omega}_{\mathcal{B}}. \end{aligned} \tag{4}$$

Here, $\boldsymbol{\Phi} = \begin{bmatrix} \varphi & \theta & \psi \end{bmatrix}^T$ denotes the Euler angles of the panel. The composition order $R = R_z(\psi)R_y(\theta)R_x(\varphi)$ was adopted for the elemental rotations to compute the rotation matrix. Then, the transformation matrix is [13]:

$$T = \begin{bmatrix} 1 & \sin\varphi\tan\theta & \cos\varphi\tan\theta \\ 0 & \cos\varphi & -\sin\varphi \\ 0 & \sin\varphi\sec\theta & \cos\varphi\sec\theta \end{bmatrix}. \tag{5}$$

In addition, $I_{\mathcal{B}}$ is the panel's inertia tensor (solid rectangular cuboid of dimensions $\boldsymbol{P}$), $\boldsymbol{\omega}_{\mathcal{B}}$ is its angular velocity observed from the rotating reference frame $\mathcal{B}$, and μ_{ω} is another friction coefficient. Equations (1)–(4) define the CDPR dynamics under gravitational, friction, and cable tensile forces. Let $x = \begin{bmatrix} \boldsymbol{r}^T & \boldsymbol{\Phi}^T & \boldsymbol{v}^T & \boldsymbol{\omega}_{\mathcal{B}}^T \end{bmatrix}^T$ be the combined state and $u = \begin{bmatrix} f_1 & \cdots & f_n \end{bmatrix}^T$ the control input. Then, the nonlinear model can be written as $\frac{d}{dt}x = h(x, u)$.

4.2 Trajectory Optimization

A general trajectory optimization problem can be formulated as minimizing a cost function while satisfying a set of constraints, including dynamics constraints, path constraints, as well as initial and terminal conditions. Consider the following cost function, formulated as the sum of the control effort and two regularization terms that ensure the smoothness of the generated motion:

$$J = \int_0^{t_T} \frac{\alpha}{N}\|\ddot{x}\|_{W_x}^2 + \frac{\beta}{N}\|\ddot{u}\|^2 \, dt. \tag{6}$$

Here, the coefficients α and β are nonnegative, N is a scaling constant equal to the number of samples observed during the trajectory, $W_x = \operatorname{diag}\begin{pmatrix} 0, & 0, & \mathbb{I}, & \mathbb{I} \end{pmatrix}$ is used for the weighted squared norm, and t_T is the terminal time. The constraints for the optimal control problem $\min_u J$ are:

Dynamic Constraints: Equations of motion

$$\frac{d}{dt}x = h(x, u), \text{ for } t \in (0, t_T) \tag{7}$$

Force Bounds: Lower bound ensures the cables only pull (sagging is allowed), while the upper bound maintains the cable tension below the rupture limit.

$$0 \leq f_i \leq f_{\max}, \forall i \in \{1, \ldots, n\} \tag{8}$$

Path Constraints: Maintain the panel inside the CDPR frame and limit both the linear and angular velocities.

$$0 \leq \boldsymbol{r} + R\mathbf{b}_{i,\mathcal{B}} \leq \boldsymbol{F}, \forall i \in \{1, \ldots, n\} \tag{9}$$

$$-\Phi_{\lim} \leq \boldsymbol{\Phi} \leq \Phi_{\lim} \tag{10}$$

$$-v_{\lim} \leq \boldsymbol{v} \leq v_{\lim} \tag{11}$$

$$-\omega_{\lim} \leq \boldsymbol{\omega}_{\mathcal{B}} \leq \omega_{\lim} \tag{12}$$

Initial Conditions: Equality constraints to ensure that the trajectory starts from $(\boldsymbol{r}_0, R_0)$ at a stationary state $\boldsymbol{v} = \boldsymbol{\omega}_{\mathcal{B}} = 0$. Let $\boldsymbol{l}_{i,0}$ be the cable vectors at $t = 0$. Then, stationary of the Newton-Euler equations (2) and (4) at the initial pickup pose becomes:

$$x_0 = \begin{bmatrix} \boldsymbol{r}_0^T & \boldsymbol{\Phi}_0^T & 0 & 0 \end{bmatrix}^T \tag{13}$$

$$0 = \begin{bmatrix} \frac{\boldsymbol{l}_{1,0}}{\|\boldsymbol{l}_{1,0}\|} & \cdots & \frac{\boldsymbol{l}_{n,0}}{\|\boldsymbol{l}_{n,0}\|} \\ \mathbf{b}_{1,\mathcal{B}} \times \frac{R_0^T\boldsymbol{l}_{1,0}}{\|\boldsymbol{l}_{1,0}\|} & \cdots & \mathbf{b}_{n,\mathcal{B}} \times \frac{R_0^T\boldsymbol{l}_{n,0}}{\|\boldsymbol{l}_{n,0}\|} \end{bmatrix} u_0 + \begin{bmatrix} m\boldsymbol{g} \\ 0 \end{bmatrix} \tag{14}$$

where x_0 and u_0 are the initial state and control. Eqn. (14) can be written in a compact matrix-vector form as $0 = A_0^T u_0 + w_p$, where A^T is referred to as the structure matrix and w_p is the stationary wrench [14].

Terminal Conditions: Equality constraints to ensure that the robot comes to a complete stop at the target pose $(\boldsymbol{r}_T, R_T)$ at time t_T. Static balance guarantees that when the robot ceases movement, the motors experience minimal stress during the stopping process:

$$x_T = \begin{bmatrix} \boldsymbol{r}_T^T & \boldsymbol{\Phi}_T^T & 0 & 0 \end{bmatrix}^T \tag{15}$$

$$0 = A_T^T u_T + w_p. \tag{16}$$

Here, x_T, u_T, A_T^T are the terminal state, terminal control, and structure matrix evaluated at t_T, respectively.

5 Simulation Results

In this section, we begin by assigning numerical values to the model parameters for simulation. Next, we present the six-cable wrench feasible workspace. Finally, we discuss the optimized trajectories for transporting the panel from a starting position to the desired final pose.

5.1 Simulation Parameters

We used a 1/3 scaled model of a three-story residential building for our simulations. The simulated cable configuration is illustrated in Figure 3. The initial and terminal poses were defined based on the expected real-world scenario. The panel was picked up from a lower height of the workspace $\boldsymbol{r}_0 = \begin{bmatrix} 0.9 & 1.0 & 0.6 \end{bmatrix}^T$ m with a pre-calculated initial orientation and zero angular and linear velocities. The panel was then held stationary at its final position at the top of the facade, fully plumb and level ($\boldsymbol{\Phi}_T = 0$). Two final positions were tested: $\boldsymbol{r}_T = \begin{bmatrix} 0.8 & 2.2 & 0 \end{bmatrix}^T$ m, and $\boldsymbol{r}_T = \begin{bmatrix} 0.8 & 2.3 & 0 \end{bmatrix}^T$ m. Here, we assume that the robot has sufficient cable length, and the cable length remains positive at all times. Other parameters and constraints are listed in Table 1. CasADi [15] was used as the numerical optimizer with a sampling time of $\Delta t = t_T / N$.

5.2 Wrench Feasible Workspace

To estimate the wrench feasible workspace $\mathcal{W}$, a set of M positions $\mathbf{r}_{j \in \{1,\ldots,M\}}$ was selected from a discretized grid. The following optimization problem was formulated to determine the optimal orientation $R_j(\boldsymbol{\Phi}_j)$ that minimizes the force vector u_j at each corresponding position:

$$\begin{aligned} &\min_{\boldsymbol{\Phi}_j} \|u_j\|^2 \quad \forall j \in \{1, \ldots, M\} \\ &\text{s.t. } 0 = A_j^T u_j + w_p, \\ &\qquad \text{Equations (8) to (10).} \end{aligned} \tag{17}$$

Table 1. Model parameters and constraints

Variable	Value	Description
m	13.6 kg	Panel mass
$\boldsymbol{F}$	$[1.83, 3.12, 1.22]^T$ m	Frame dimensions
$\boldsymbol{P}$	$[0.76, 0.76, 0.25]^T$ m	Panel dimensions
μ_v	100 kg/s	Linear friction coefficient
μ_ω	3500 kg · m^2/s	Angular friction coefficient
$f_{\max}$	1200 N	Cable maximum force
$\boldsymbol{\Phi}_{\lim}$	90 deg	Euler angle limit
$\boldsymbol{v}_{\lim}$	0.2 m/s	Linear velocity limit
$\boldsymbol{\omega}_{\lim}$	2 deg/s	Angular velocity limit
t_T	20 s	Terminal time
N	2000	Samples per trajectory

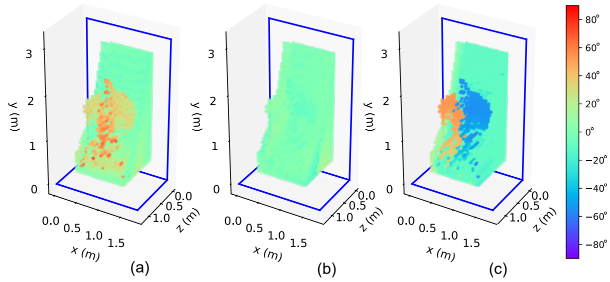

Figure 4. Plots (a), (b), and (c) represent the optimal Euler angles $\boldsymbol{\Phi}_j = [\varphi_j \quad \theta_j \quad \psi_j]^T$, respectively.

If the optimizer converges to a solution, the pose $(\mathbf{r}_j, R_j)$ is wrench-feasible. Figure 4 illustrates the optimized Euler angles $\boldsymbol{\Phi}_j$. The main region of $\mathcal{W}$ resembles a wedge shape and the majority of angles fall within [-20°, 20°]. Note that $\mathcal{W}$ connects the facade installation plane with the assumed pickup panel locations (away from the facade and close to the ground). Thus, there should exist feasible continuous trajectories that can transport the end effector from its starting pose to the installation plane within $\mathcal{W}$. Moreover, we can find trajectories that satisfy certain optimal criteria to minimize installation time and effort.

5.3 Optimized Trajectories

Given the start position $\mathbf{r}_0$ and the final desired pose $(\mathbf{r}_T, R_T)$, we use the trajectory optimization method described in Section 4.2 to compute the optimal force trajectory for the CDPR to follow in simulation. In trajectory optimization, finding a suitable initial trajectory is critical for accelerating the convergence of the optimizer. For the six-cable configuration, finding a suitable initial trajectory is particularly challenging. Firstly, achieving an initial plumb and level orientation $\boldsymbol{\Phi}_0 = 0$ is generally infeasible for most points in the workspace. In contrast, for the eight-cable CDPR, the end effector can be assumed to start in a plumb and level position or with small random rotations.

Consequently, determining an appropriate initial orientation for a given starting position is nontrivial and requires a dedicated optimization process. Selecting an improper orientation—even if wrench-feasible—can lead to convergence failure during optimization. Secondly, generating a practically feasible initial trajectory from the given starting pose to a position near the goal is another significant challenge. The trajectory should ideally satisfy feasibility criteria while avoiding abrupt discontinuities in inputs or states. Unlike in the eight-cable CDPR, where the initial trajectory can be directly obtained using inverse dynamics, the six-cable system requires a more intricate approach to ensure smooth and feasible motion. We address these two challenges in the following paragraphs.

5.3.1 Determining the orientation of the starting pose

To determine the orientation of the starting pose, we first generate a linear static trajectory connecting the initial and terminal positions: $\{\boldsymbol{r}_0, \boldsymbol{r}_1^\dagger, \ldots, \boldsymbol{r}_k^\dagger, \ldots, \boldsymbol{r}_{T-1}^\dagger, \boldsymbol{r}_T\} \in \mathcal{W}$. At the goal pose $(\boldsymbol{r}_T, \boldsymbol{\Phi}_T)$, an optimization routine similar to Eqn. (17) can be done to find the optimal input force $u_T^\dagger$ by solving $\min_u \|u_T\|^2$. Then, starting from the goal pose and moving backwards along the position trajectory, the optimal orientation $\boldsymbol{\Phi}_k^*$ and input force $u_k^\dagger$ at the k-th ($0 \leq k < T = N - 1$) pose is calculated using the constraints in Eqn. (17) and the following cost function:

$$\min_{\boldsymbol{\Phi},u} \gamma_\Phi \|\boldsymbol{\Phi}_k - \boldsymbol{\Phi}_{k+1}\|^2 + \gamma_u \|u_k - u_{k+1}\|^2. \tag{18}$$

Here, γ_Φ and γ_u are weighting factors. The cost function was designed to ensure continuity in both orientation and control input. This optimization is performed position by position, progressing backward until the starting position is reached, as depicted in Figure 5. The resulting optimal continuous quasi-static force trajectory $\{u_0^\dagger, \ldots, u_T^\dagger\}$ is shown at the top plot of Figure 6. Note that the final force values of two cables are zero (cables 1 and 4 start sagging), signaling the transition from a six-cable 3D CDPR system to a four-cable 2D CDPR system. The optimized $\boldsymbol{\Phi}_0^*$ is then set as the orientation for the starting pose.

5.3.2 Generating initial trajectories for the optimizer

Having a well-defined initial trajectory is crucial for accelerating the convergence of the optimizer. Using the starting pose $(\boldsymbol{r}_0, \boldsymbol{\Phi}_0^*)$, static conditions $\boldsymbol{v} = \boldsymbol{\omega}_{\mathcal{B}} = 0$, and quasi-static force trajectory $\{u_0^\dagger, \ldots, u_T^\dagger\}$ as inputs, we applied the system dynamics in Eqn. (7) to compute the dynamic state trajectory. The bottom plots in Figure 6 compare the dynamic trajectory (solid line) with the quasi-static trajectory (dashed line) used in the backwards optimization. Note that the final pose of the dynamic state trajectory does not coincide with the desired target pose.

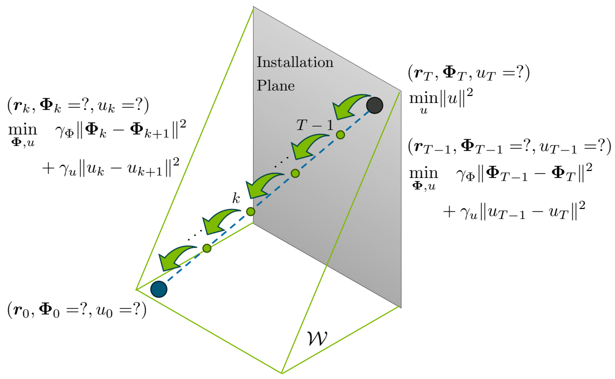

Figure 5. Backwards optimization for finding initial orientation $\boldsymbol{\Phi}_0^*$ and force trajectory $\{u_0^\dagger, \ldots, u_T^\dagger\}$

This occurs because the backward optimization was performed using static instead of dynamic constraints. This simplification impacts the results accuracy, as it fails to account for changes in velocity and acceleration. This dynamic state trajectory was used to initialize the optimizer.

In practice, two routing strategies can be used to generate the initial trajectory. The first method, directly connecting the start and end positions, was described in Section 5.3.1. However, this approach does not guarantee that Eqn. 18 will converge at every point along the trajectory. To address this issue, we propose a second approach that divides the process into two phases. In the first phase, the end effector is moved to a position on the installation plane, which can be selected near the initial position (similar heights). Once the end effector reaches the plane, cables 1 and 4 are slackened, transforming the system into a 2D planar configuration. Each phase's trajectory is optimized separately, and the two optimized segments are concatenated to form the initial trajectory. This trajectory is then used by the optimizer to find the final optimal trajectory from the true starting position to the desired pose.

5.3.3 Final optimized trajectories

Figure 7 illustrates two optimal trajectories originating from the same starting position but with different initial orientations. In the left plot, the trajectory used to initialize the optimizer directly connects the start and end positions. In contrast, the right plot demonstrates an initial trajectory that first guides the end effector to the installation plane before moving upwards along the plane. The reason for splitting the trajectory in the second example is that the optimizer failed when attempting to conduct the backwards optimization to find the optimal orientation for the initial position. As a result, the initial trajectory for the second example first brings the end effector to the position $\begin{bmatrix} 0.8 & 1.2 & 0 \end{bmatrix}^T$ m, before continuing to the final goal

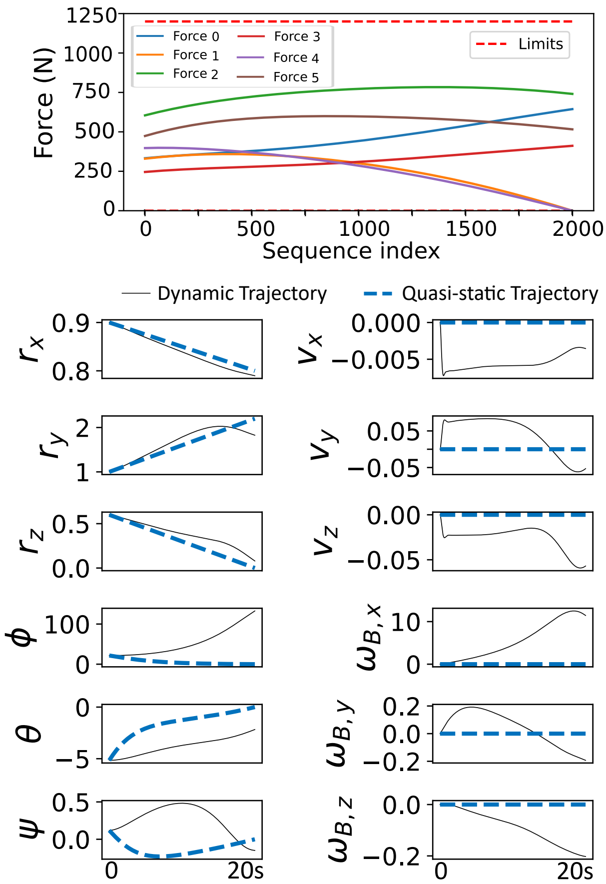

Figure 6. Example of calculated initial trajectory. Top: quasi-static force trajectory calculated using backward optimization. Bottom: comparison between quasi-static and dynamic trajectories. Positions are measured in meters and angles in degrees.

pose.

Although the left plot in Fig. 7 shows a shorter Euclidean distance between $\boldsymbol{r}_0$ and $\boldsymbol{r}_T$ compared to the right plot, the CasADi optimizer achieved only an acceptable level of convergence in the left case, while it successfully reached the optimal solution in the right case. This may explain why the linear velocity profile in the right plot is smoother than that in the left plot. After the optimizer converges, both methods lead to smooth force input trajectories $\{u_0^*, \ldots, u_T^*\}$. The top plots of Fig. 7 show the optimal input force. In method one (left plot), all six cables are used until the end effector reaches the installation plane, then only four cables are used. On the other hand, method two (right plot) achieves the same goal with a lower average input force, as it tends to sag at least one cable throughout most of the trajectory. Although splitting the trajectory into two phases requires running the trajectory optimization process three times: first to bring the end effector to the installation plane, then to travel within

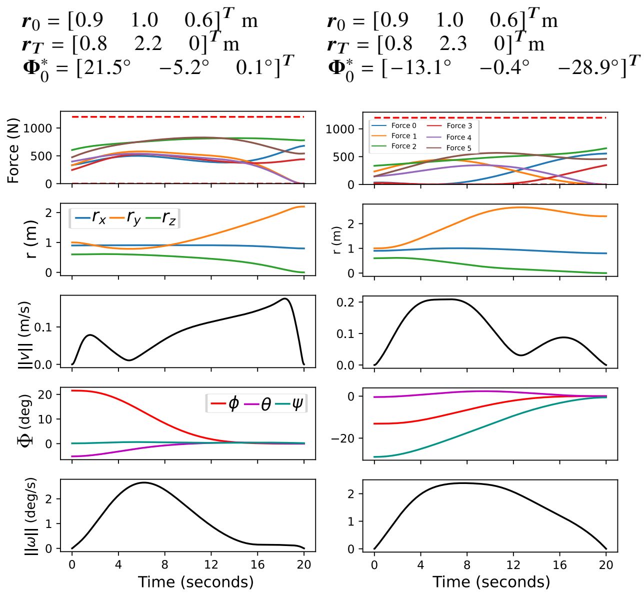

Figure 7. Two optimized trajectories starting from the same position with different initial orientations.

the plane, and finally to optimize the trajectory for the final pose, the process proves more practically feasible as it is more robust and converges faster.

6 Conclusion and Future Work

This paper investigated the feasibility of employing a six-cable CDPR for panelized building retrofits, with the goal of simplifying the robot installation and setup process, reducing costs, and simultaneously maintaining the essential functionalities required for building retrofits. Through simulation, we examined one specific cable arrangement, evaluated its wrench feasible workspace, and optimized trajectories within this workspace to transport the end effector from a starting position to the desired goal pose. Given the initial panel pickup position $\boldsymbol{r}_0$, desired panel position $\boldsymbol{r}_T$, and assuming that the panel will be installed plumb and level $\boldsymbol{\Phi}_T = 0$, the proposed method determines the optimal pickup orientation $\boldsymbol{\Phi}_0^*$ and computes the optimal continuous input force trajectory $\{u_0^*, \ldots, u_T^*\}$ that minimizes cable force, maintains the system within safe boundaries, and achieves the desired terminal pose.

This work primarily focuses on studying the feasibility of the six-cable CDPR in a construction setting, specifically investigating whether a dynamically feasible path exists to transport the panel from the bottom to the top. However, we do not address other real-world challenges, such as partial observability or external disturbances, which can significantly impact system performance. These aspects require further exploration and will be our future work.

Additionally, this study did not consider cable-to-cable collisions. Future research will address this limitation by exploring methods to adjust the positions of the anchors in order to avoid such collisions. Moreover, in the six-cable model, two cables must sag as the end effector nears the installation plane. Moving forward, we aim to investigate the sagging mechanism to better understand its effects on system stability and performance. Furthermore, We also plan to explore how the system can be adapted to handle larger-scale applications and more complex scenarios.

ACKNOWLEDGMENT

This research was supported by the DOE Office of Energy Efficiency and Renewable Energy (EERE), Building Technologies Office, under the guidance of Sven Mumme, and used resources at the Building Technologies Research and Integration Center, a DOE-EERE User Facility at Oak Ridge National Laboratory. Research also sponsored by the Laboratory Directed Research and Development Program of Oak Ridge National Laboratory, managed by UT-Battelle, LLC, for the U. S. Department of Energy.

References

[1] Christian Mascheck. Serielles sanieren: So funktioniert der "energiesprong". Online: `https://cradle-mag.de/artikel/serielles-sanieren-energiesprong.html`, Accessed: 12/19/2024.

[2] Jean-Baptiste Izard, Alexandre Dubor, et al. Large-scale 3d printing with cable-driven parallel robots. *Construction Robotics*, 1:69–76, 2017.

[3] Tobias Bruckmann, Wildan Lalo, et al. Development of a storage retrieval machine for high racks using a wire robot. In *International Design Engineering Technical Conferences and Computers and Information in Engineering Conference*, volume 45035, pages 771–780. American Society of Mechanical Engineers, 2012.

[4] Yifang Liu, Rui Zhang, et al. Cable-driven parallel robot (cdpr) for panelized envelope retrofits: Feasible workspace analysis. In *ISARC. Proceedings of the International Symposium on Automation and Robotics in Construction*, volume 41, pages 1081–1088, 2024.

[5] Kepa Iturralde, Malte Feucht, et al. Cable-driven parallel robot for curtain wall module installation. *Automation in Construction*, 138:104235, 2022.

[6] Tobias Bruckmann, Christopher Reichert, et al. Concept studies of automated construction using cable-driven parallel robots. In Clément Gosselin, Philippe Cardou, Tobias Bruckmann, and Andreas Pott, editors, *Cable-Driven Parallel Robots*, pages 364–375, Cham, 2018. Springer International Publishing. ISBN 978-3-319-61431-1.

[7] Paul Bosscher, Robert L. Williams, et al. Cable-suspended robotic contour crafting system. *Automation in Construction*, 17(1):45–55, 2007. ISSN 0926-5805.

[8] Sen Qian, Changqi Li, et al. Modeling and experimental validation of a cable-driven robot for three-dimensional printing construction. *Journal of Mechanisms and Robotics*, 17(6), 2025.

[9] Andreas Pott, Christian Meyer, and Alexander Verl. Large-scale assembly of solar power plants with parallel cable robots. In *ISR 2010 (41st International Symposium on Robotics) and ROBOTIK 2010 (6th German Conference on Robotics)*, pages 1–6. VDE, 2010.

[10] Kevin Murphy, Joao CV Soares, et al. Cooperative modular manipulation with numerous cable-driven robots for assistive construction and gap crossing. *arXiv preprint arXiv:2403.13124*, 2024.

[11] Jean-Baptiste Izard, Marc Gouttefarde, et al. *Integration of a Parallel Cable-Driven Robot on an Existing Building Façade*, pages 149–164. Springer Berlin Heidelberg, Berlin, Heidelberg, 2013. ISBN 978-3-642-31988-4.

[12] R. C. Hibbeler. *Engineering Mechanics Dynamics*. Pearson, New Jersey, 11th edition, 2007. ISBN 0-13-221504-7.

[13] Robert McGhee, Eric Robert Bachmann, et al. Rigid body dynamics, inertial reference frames, and graphics coordinate systems: A resolution of conflicting conventions and terminology. 2000.

[14] Andreas Pott and Tobias Bruckmann. *Cable-driven parallel robots*. Springer, 2013.

[15] Joel A E Andersson, Joris Gillis, et al. CasADi – A software framework for nonlinear optimization and optimal control. *Mathematical Programming Computation*, 11(1):1–36, 2019.